Widespread deep seismicity in the Delaware Basin, Texas, is mainly driven by shallow wastewater injection

Guang Zhai[a,b,c,1], Manoochehr Shirzaei[c,1], and Michael Manga[a,b,1]

[a]Berkeley Seismological Laboratory, University of California, Berkeley, CA 94720; [b]Department of Earth and Planetary Science, University of California, Berkeley, CA 94720; and [c]Department of Geosciences, Virginia Polytechnic Institute and State University, Blacksburg, VA 24061

Contributed by Michael Manga, March 29, 2021 (sent for review February 4, 2021; reviewed by Timothy H. Dixon and Shemin Ge)

Industrial activity away from plate boundaries can induce earthquakes and has evolved into a global issue. Much of the induced seismicity in the United States' midcontinent is attributed to a direct pressure increase from deep wastewater disposal. This mechanism is not applicable where deep basement faults are hydraulically isolated from shallow injection aquifers, leading to a debate about the mechanisms for induced seismicity. Here, we compile industrial, seismic, geodetic, and geological data within the Delaware Basin, western Texas, and calculate stress and pressure changes at seismogenic depth using a coupled poroelastic model. We show that the widespread deep seismicity is mainly driven by shallow wastewater injection through the transmission of poroelastic stresses assuming that unfractured shales are hydraulic barriers over decadal time scales. A zone of seismic quiescence to the north, where injection-induced stress changes would promote seismicity, suggests a regional tectonic control on the occurrence of induced earthquakes. Comparing the poroelastic responses from injection and extraction operations, we find that the basement stress is most sensitive to shallow reservoir hydrogeological parameters, particularly hydraulic diffusivity. These results demonstrate that intraplate seismicity can be caused by shallow human activities that poroelastically perturb stresses at hydraulically isolated seismogenic depths, with impacts on seismicity that are preconditioned by regional tectonics.

induced seismicity | hydrocarbon recovery | wastewater

Seismicity induced by anthropogenic activities has become increasingly widespread globally, representing a growing hazard over the past decade (1–3). In the United States, much of the recent increase in induced seismic activity has been linked to a dramatic increase in the disposal of wastewater into deep aquifers (3–6), where the injected fluid can diffuse downward into the hydraulically connected underlying basement at seismogenic depth (7–9). A much smaller number of events can be attributed directly to hydraulic fracturing (6). However, many disposal wells that target shallow hydraulically isolated aquifers, vertically distant from the basement, are also statistically associated with induced earthquakes (10, 11). This observation calls into question the role of injection depth in the occurrence of induced seismicity (10, 12). Despite extensive studies of injection in deep aquifers, the mechanisms of induced basement earthquakes due to shallow injection are poorly understood.

The Permian Basin, TX, has a long history of hydrocarbon production and is among the most productive shale basins for fossil fuel extraction in the United States (11). The seismicity surge since 2014 within the Delaware Basin, a subbasin in the western Permian Basin, is related to unconventional shale oil and gas extraction (13). However, a deterministic physical process that induces basin-wide seismicity remains unclear (13, 14). Considering that most fluid injection occurs in hydraulically isolated shallow aquifers (15), the observation of basin-wide induced seismicity provides an opportunity to investigate new mechanisms governing the interaction between shallow injection and deeper seismicity.

Results

Fig. 1 shows the distribution of wastewater injection and oil and gas extraction sites within the Delaware Basin. Since 2010, hydraulic fracturing became widespread for stimulating shale plays (*SI Appendix*, Figs. S1 and S2). We compiled the reported wastewater injection and oil and gas extraction volumes provided by the TX Railroad Commission for 2010 to 2020, comprising 478 injection (only 9 injecting below 4.5 km) and 1,971 production high-volume wells (Fig. 1*A* and *SI Appendix*, SI Text). The wells' reported production values are an approximation for each oil and gas lease (*SI Appendix*, SI Text). During this period, a total of ∼0.7 and 0.6 km^3 of wastewater and hydrocarbon were injected and produced, with ∼94 and 99% of injected and produced volume during 2014 to 2020, respectively (Fig. 1*B*). We acquired the original earthquake catalog from the TexNet Seismic Monitoring, which has recorded earthquakes since 2017 (16). In total, 446 $M \geq 2.0$ events, including the M5.0 event on 26 March 2020 (17, 18), were recorded in our study area (Fig. 1 and *SI Appendix*, Fig. S3). Only a small cluster of these earthquakes are linked to short-term hydraulic fracturing (14, 19), implying that most of the events are associated with wastewater disposal and hydrocarbon extraction.

The Delaware Basin's subsurface is characterized by a thick shale reservoir at 2 to 4.5 km depth, separating the overlying 1.3-km-thick permeable Delaware sandstone that hosts the wastewater injection

Significance

The Delaware Basin, western Texas, has experienced a surge in the number of earthquakes. We investigate basin-wide earthquake, hydrogeologic, industrial, and geodetic data spanning 1993–2020 to identify the reasons for the increase. We use these data and models to quantify the stress changes from wastewater injection and hydrocarbon extraction. We demonstrate that the basin-wide seismicity is dominated by the stresses caused by shallow injection that are transmitted vertically by deforming the underlying crust. We analyze both injection and production data to understand how subsurface properties control earthquake locations and timings. We suggest that injecting wastewater into porous formations will minimize seismic hazard. We establish a framework explaining why earthquakes sometimes occur and sometimes do not occur within human activity-impacted areas.

Author contributions: G.Z., M.S., and M.M. designed research; G.Z. and M.S. performed research; G.Z. and M.S. analyzed data; and G.Z., M.S., and M.M. wrote the paper.

Reviewers: T.H.D., University of South Florida; and S.G., University of Colorado Boulder.

The authors declare no competing interest.

[1]To whom correspondence may be addressed. Email: gzhai@seismo.berkeley.edu, shirzaei@vt.edu, or manga@seismo.berkeley.edu.

This article contains supporting information online at https://www.pnas.org/lookup/suppl/doi:10.1073/pnas.2102338118/-/DCSupplemental.

Published May 10, 2021.

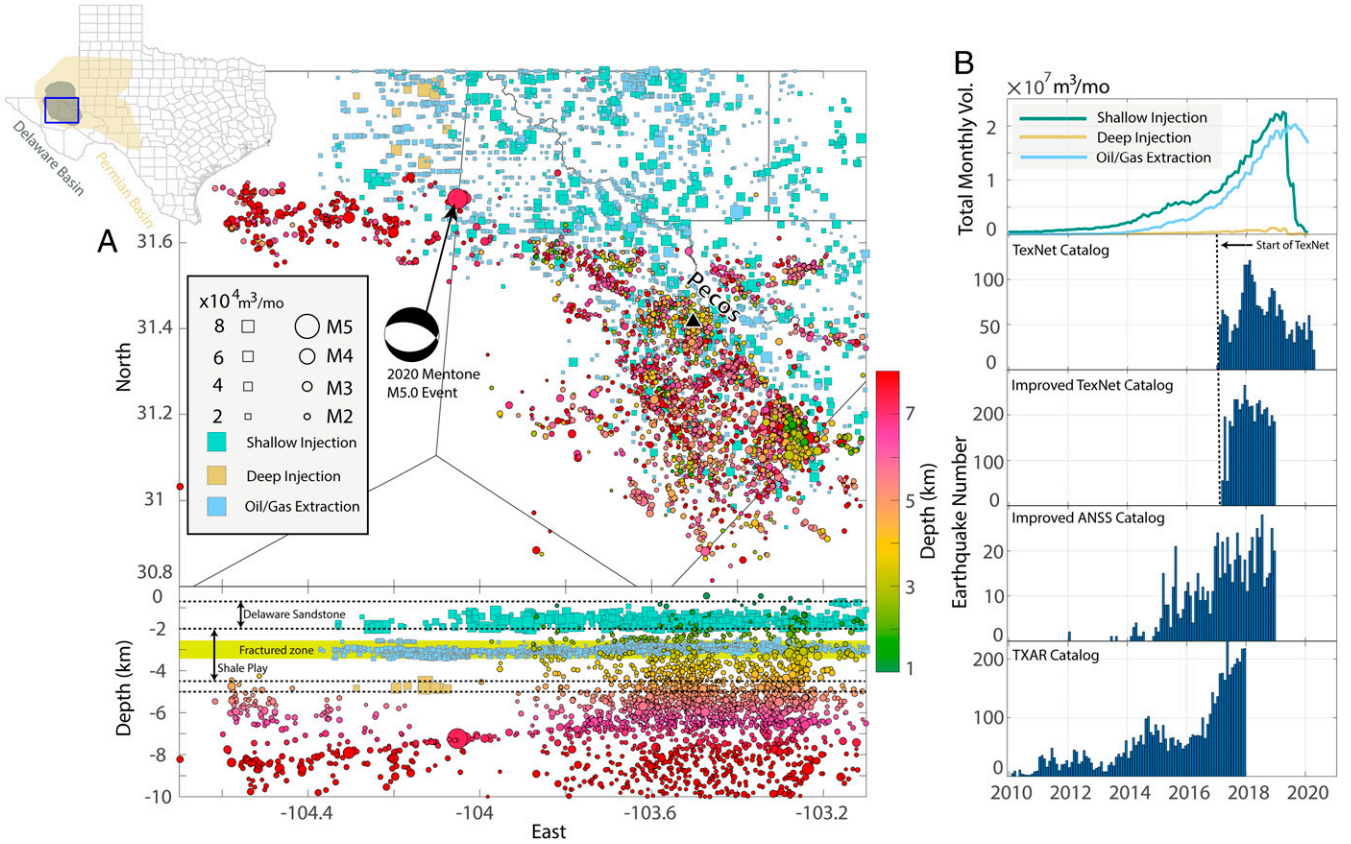

Fig. 1. Industrial and seismic activities within the Delaware Basin, TX. (*A*) Map and cross-section views of the spatial distributions of disposal wells, production wells, and declustered original TexNet earthquakes with foreshocks and aftershocks removed. The earthquake and well depths in the layered model are corrected relative to the Delaware sandstone formation bottom as a vertical reference (*SI Appendix*, SI Text). Black lines are the county boundaries. Black triangle indicates the location of the town of Pecos. (*Inset*) The location of the study area. (*B*) Temporal evolution of recorded injection and production volumes and four different declustered catalogs within the study area. The catalogs include the original TexNet catalog and improved TexNet and ANSS catalogs made by template matching (14) and TXAR catalog (13).

and the underlying basement where a large number of earthquakes occur (Fig. 1*A*). The declustered TexNet earthquake and well depths, shown in Fig. 1*A*, are corrected with respect to the Delaware sandstone formation bottom as a vertical reference (*SI Appendix*, SI Text). Oil and gas extraction originate from a narrow zone embedded within the overall low-permeability shale reservoir, as shown by the production well depth distribution (Fig. 1*A*). This production zone is extensively fractured with an enhanced permeability (*SI Appendix*, SI Text). Considering that the length of hydraulic fractures is mostly less than 200 m (20, 21), the unfractured, extremely low-permeability shales should reasonably sandwich the fractured zone as cap or buffer layers over the decadal time scale (20) and avoid an effective hydraulic communication between the deep basement and the shallow sandstone and fractured shale. This suggests that direct pore pressure diffusion is unlikely to be the primary driver of most basin-wide seismicity observed in the Delaware Basin. Further, there is no measurable temporal delay between the evolution of declustered seismicity and fluid injection and production (Fig. 1*B*), implying a dominant simultaneous seismic response at the basin-wide scale, despite the temporal delays possibly observed at local scales (22). The other declustered seismic datasets include the improved TexNet and Advanced National Seismic System (ANSS) catalogs made by template matching (14) and TXAR catalog (13) that extend the TexNet catalog in time (Fig. 1*B*). These observations collectively indicate that basement and shallow reservoirs interact elastically over decadal time scales. In addition to the injection-induced slip (23, 24), both poroelastic coupling between fluid and solid materials (25–28) and gravitational loading (29) can transmit elastic stress changes beyond the pressurized zone.

To quantify the diffusion processes from sandstone injection and shale extraction and investigate the link to observed seismicity, we build a linear, layered poroelastic model to investigate the spatiotemporal distribution of poroelastic stresses and pore pressure at the seismogenic depth of 5 km within the basement (*SI Appendix*, Figs. S4–S6). This model is constrained by subsurface stratigraphy, local hydrogeology, and seismic tomography (*SI Appendix*, SI Text). Essentially, it describes the coupled fluid flow processes within the injection and extraction reservoirs, whose expansion and contraction determine the poroelastic response at depths where earthquakes occur. Within the reservoirs, fluid diffusion is controlled by hydraulic diffusivity. The Delaware sandstone is hydrogeologically distinct from the shale reservoir (Fig. 1*A*). Based on laboratory experiments on a wide range of different sandstones, the value of sandstone diffusivity is typically between 0.1 and 1.0 m^2/s (30–32), with a choice of 0.5 m^2/s for the Delaware sandstone in our model (*SI Appendix*, Table S1). Fluid diffusion associated with shale extraction is primarily determined by hydraulic fracturing operations (33), significantly increasing the effective reservoir permeability by enhancing fracture networks' connectivity, enabling oil and gas production (*SI Appendix*, SI Text). The fractured shale is characterized by large pathway permeability, suggesting an effective diffusivity larger than 10 m^2/s and up to two orders of magnitude larger (34), with the lower bound used for the poroelastic modeling.

Using the Earth model and time series of injected and extracted fluid volume, we solve for the spatiotemporal evolution of the

pore pressure and poroelastic stresses in the crust (*SI Appendix*, Figs. S7 and S8). Owing to the high water to hydrocarbon ratio for the Permian shale, the actual extraction volume includes the coproduced wastewater (11). Assuming that the regionally produced water volume is balanced with wastewater disposal, which is comparable to the volume of hydrocarbon production (Fig. 1*B*), we linearly scale the hydrocarbon volume with a factor of 2 at all production sites to inform the poroelastic model. We calculate the cumulative Coulomb failure stress (CFS) contribution separately due to changes in poroelastic stresses and pore pressure in order to identify the dominant contribution to the CFS. The normal-faulting focal mechanism of the M5.0 event with strike = 285°, dip = 56°, and rake = −77° is consistent with regional tectonic stresses (17, 35). This geometry is used to calculate the CFS with a friction coefficient of 0.6. For both fluid injection and extraction, poroelastic stresses dominate the spatial distribution of CFS change rather than pore pressure (*SI Appendix*, Fig. S7). The imparted CFS change due to poroelastic stresses caused by injection is positive (promotes failure), while that from extraction is negative (*SI Appendix*, Fig. S7). This is because injection and extraction cause horizontal rock extension and compression, respectively, below reservoirs (25, 36, 37), and the regional tectonic stress regime is extensional (35). Interestingly, due to poroelastic coupling, the disposal injection leads to negative pore pressure change at depth in contrast to the effects of shale extraction, assuming the basement is fluid-saturated with low diffusivity. This pattern of pore pressure results from rock volumetric increase due to imparted poroelastic stresses. Similar behavior is observed at other pumping test sites due to fluid–solid coupling (27, 37, 38). Note that for injection into the deep layer that may be hydraulically connected to the basement through preexisting fractures, the additional effect of downward fluid diffusion may increase the pore pressure on basement faults at local scales, which was proposed to contribute to the basement M5.0 event (18).

Superimposing both poroelastic stresses and pore pressure changes, we obtain maps of the total CFS for each type of well and their cumulative effect (Fig. 2 *A*–*C*). We observe that the deep injections only have a local impact, while the effects from shallow injections dominate the total CFS distribution over shale extractions (Fig. 2*D*). The magnitude of total CFS is up to 1 Bar. The Delaware Basin's seismicity occurs within the area that receives positive CFS change, suggesting a basin-wide causal link between shallow injection and deeper seismicity (Fig. 2*D*). Calculation of CFS considering the different receiver fault strikes and depths further confirms the robustness of this basin-wide link (*SI Appendix*, Figs. S9 and S10).

The reservoir fluid diffusion process can explain the different mechanical responses at depth to sandstone injection and shale extraction. The reservoir pore pressure (Δp) and poroelastic stresses ($\Delta\sigma$) are coupled through the following relationships (26, 32):

$$\Delta p \propto \frac{f_p(\zeta)}{D\alpha^2} \quad , \quad \Delta\sigma \propto \frac{f_s(\zeta)}{D\alpha},$$

where D is the hydraulic diffusivity, α is the Biot's effective stress coefficient, and $\zeta = r/\sqrt{Dt}$ is the normalized variable of distance r and time t. $f_p(\zeta)$ and $f_s(\zeta)$ are the kernel functions describing the patterns of pore pressure and poroelastic stresses within the reservoirs. Larger poroelastic coupling ($\frac{\Delta\sigma}{\Delta p} \propto \alpha$) results in both smaller reservoir pore pressure and stress buildup. The reservoir expansion and contraction associated with injection and extraction layers are described by the effective reservoir stress $\Delta\sigma + \alpha\Delta p \propto 1/D\alpha$ (32). For permeable formations (i.e., large D), larger poroelastic coupling and fluid movement lead to less effective rock deformation. This means that compared with fractured shale, the fluid volume change within the sedimentary sandstone characterized by a slower fluid flow causes a larger change in bulk effective stresses and rock deformation (Fig. 2). Thus, even though the sedimentary sandstone in the Delaware Basin may be farther from the hypocenters than the shale, it has a larger effect on stresses and induced earthquakes due to its hydrogeological properties.

To further test the mechanical control on stresses and seismicity, we examine the basin-wide surface deformation that could provide clues on subsurface stress changes linked to fluid injection

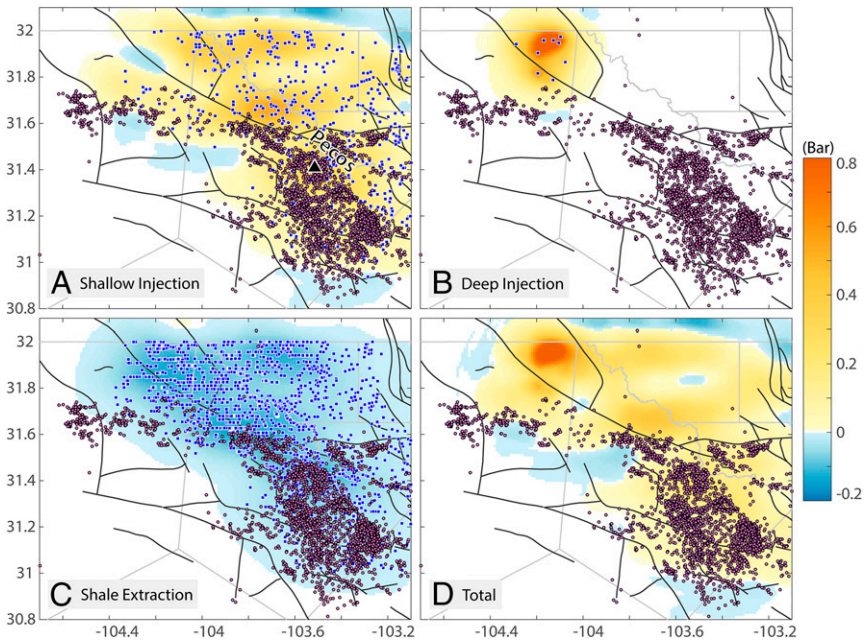

Fig. 2. Cumulative total CFS from poroelastic stresses and pore pressure at seismogenic depth (5 km) within the basement during 2014 to 2020. (*A*) CFS for shallow sandstone injection. (*B*) CFS for deep Ellenberger injection. (*C*) CFS for shale extraction. (*D*) The sum of *A*–*C*. Dark curves show the faults. Blue squares show the well locations for the corresponding well types. Purple circles indicate the declustered TexNet earthquake epicenters.

and production (Fig. 3). We apply a multitemporal synthetic aperture radar (SAR) interferometric analysis to C-band SAR images in descending path acquired by Sentinel-1A/B satellites over the Delaware Basin between September 2016 and December 2020 (*Methods*), during which fluid injection and production are the largest. The interferometric SAR (InSAR) line-of-sight (LOS) velocity map is shown in Fig. 3. The southern deformation (latitude ~31.4) pattern is similar to that of published studies (22, 39) and is characterized by land subsidence up to 3 cm/yr where the injection and production wells colocate and injection volume is larger than that of production. Given the shallower depth of injection in the Delaware Basin and that the sandstone layer is more susceptible to deformation due to injection, a surface uplift caused by sandstone injection is expected to dominate the subsidence caused by shale extraction. However, groundwater extraction from the shallow and semiconfined (largely unconfined) Pecos Valley (PV) aquifer causes an additional subsidence signal (40). Fig. 3 is characterized by a faster subsidence rate where the water table is shallow and the aquifer is thick (41), indicating that the observed subsidence is primarily caused by shallow groundwater extraction (40) rather than reservoir compaction (22, 39). In the northern section (seismic quiescence zone, latitude ~31.8) where there is little impact due to PV aquifer compaction, the deformation map shows both surface uplift and subsidence that correlate with the injection and production well locations, respectively. Note that in the north, the production and injection sites are mostly separated spatially, in contrast to the southern region. Thus, our deformation analysis demonstrates that shallow injection can cause surface uplift and shallow subsurface pressure and stress buildup that could dominate CFS in the seismogenic basement, as shown in Fig. 2.

The deformation analysis is consistent with poroelastic processes affecting stresses and thus seismicity at depth. However, there are regions of seismic quiescence to the north that experience large positive CFS (Fig. 2). The extraction volume from conventional reservoir exploitation prior to 2010 is too small to have depleted the stress at depth (*SI Appendix*, Fig. S2), although this process was suggested to be the reason for the northern seismic quiescence (42). Thus, this observation implies that faults may be less abundant to the north or preexisting basement faults are not critically stressed due to the regional stress rotation and heterogeneity (35), consistent with previous results suggesting that injection has not exceeded a threshold (22). Thus, our analysis highlights the importance of mapping tectonic faults and quantifying regional stresses for a realistic assessment of seismic hazards associated with fluid injection.

Additionally, fluid injection and extraction cause regional mass changes. Mass changes produce an elastic response and modify the stress at depth due to gravitational loading (43), contributing to induced seismicity (29, 44). The net change in volume of fluid in the Delaware Basin is comparable to that of seasonal groundwater volume change in Central Valley, CA, where hydrological loading modulates seismicity on nearby faults (44, 45). To investigate the loading effect of wastewater injection and hydrocarbon extraction in the Delaware Basin, we calculate the time-dependent stress variations at the same seismogenic depth (*SI Appendix*, SI Text). Using the same receiver fault geometry and friction coefficient, the cumulative CFS distribution due to fluid mass change has an intricate pattern and is mostly negative at earthquake epicenters (*SI Appendix*, Fig. S11) since the net mass loss causes compression at depth. The magnitude of CFS is up to 0.01 Bar (1 kPa) and is about two orders of magnitude smaller than poroelastic stresses, implying that the loading effect due to mass change is not responsible for the induced seismicity in the Delaware Basin.

Discussion and Conclusions

Our analysis suggests that shallow injection and poroelastic processes dominate the stress distribution at depth and are responsible for most of the induced seismicity in the Delaware Basin at the basin scale. Heterogeneity, however, may perturb the inducing process at the local scale (22). Alternatively, preexisting fractures could act as pathways that provide hydraulic connectivity between the shallow sandstone and deep basement faults. The prevalence of such fractures is unlikely because they would lead to significant oil and gas leakage to contaminate the shallow aquifers, which is

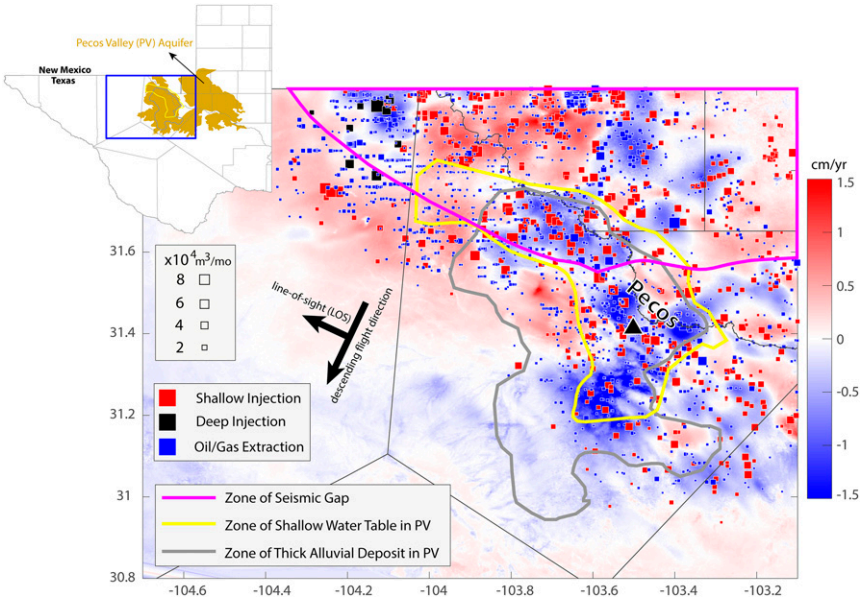

Fig. 3. Deformation map showing the distribution of SAR LOS velocity between 2016 and 2020. Red and blue colors indicate the surface movement toward and away from the satellite, respectively. (*Inset*) The footprint of the PV aquifer as well as the study area. Magenta curve shows the seismic quiescence zone following Fig. 2 and *SI Appendix*, Fig. S2. Yellow and gray curves are the approximate zones of the shallow water table and thick alluvial deposit in PV, respectively (41). Squares indicate the well locations, with symbol sizes scaled by average monthly well volumes during the same observation period as the deformation.

not reported. Although we favor unfractured shales as cap or buffer layers acting as hydraulic barriers, we cannot rule out the possibility that the injected wastewater in shallow sandstone may diffuse through the shale reservoir to induce seismicity (22). However, this process requires that the shale reservoir is hydraulically connected to the underlying formations. In this case, petroleum extraction would significantly decrease the pore pressure within both the shale and basement, causing basin-wide pressure deficits and thus long delays between the beginnings of injection and seismicity, which is not observed at the basin scale. Testing these scenarios would benefit from future in situ permeability and pore pressure measurements that document the permeability structure and evolution of the extensively fractured shale reservoir. Furthermore, the hypocenter uncertainty of the TexNet catalog may shift the recorded seismicity a couple of kilometers vertically (16). However, induced earthquakes (excluding those from hydrofracturing) in the Permian Basin are more likely to occur in the unfractured shale or basement. The fractured production zone undergoes a pressure decrease, and the shallow Delaware sandstone probably has rate-strengthening frictional properties, thus is unlikely to host significant seismicity (7) although wastewater injection formations are possible locations for earthquake nucleation (46).

Determining the dominant mechanism that controls injection-induced seismicity is essential. Unlike the effect of pore pressure changes that is independent of fault geometry, the role of poroelastic stresses in inducing seismicity and assessing the associated seismic hazard is not as straightforward to understand. Poroelastic stresses can hinder or enhance the effect of direct pore pressure changes depending on subsurface hydrogeological properties and fault architectures (9, 36, 47). Forecasting injection-induced seismicity, e.g., in Oklahoma where basement faults are hydraulically connected to the targeted reservoir (48), has evolved from an empirical model that ignores poroelastic effects (49) to physics-based models that couple poroelastic stresses and pore pressure evolution (47). However, it remains debated whether poroelastic stresses alone could dominate the process of induced seismicity in petroleum-producing areas (9, 28, 47). Because the amplitude of poroelastic stresses decays exponentially with distance (26), it remains an open question whether CFS changes from poroelastic stresses can encourage earthquakes over distances greater than tens of kilometers. Previous studies show that poroelastic stresses can enhance seismicity in conventional oil and gas fields (25, 37). Here we show that the contributions from poroelastic stresses alone can dominate the process of induced seismicity in an unconventional field through vertical poroelastic interactions, where there is little to no hydraulic connectivity.

Injection-induced seismicity is generally attributed to the reactivation of deep basement faults, which is driven by pressure diffusion and stress transmission (3, 50). Pore pressure diffusion requires hydraulic connectivity between the injection aquifer and seismogenic fault. However, stress transmission can elevate the CFS and induce earthquakes despite insignificant fluid diffusion to hypocenters due to the large distance or low permeability (51). Our compilation and analysis of regional fluid injection and extraction in the Delaware Basin permit a better understanding of the physical mechanism and mechanical control on induced seismicity (Fig. 4). Within a petroleum-producing area, both wastewater injection and hydrocarbon extraction lead to fluid redistribution and fluid–solid coupling. With limited hydraulic communication between shallow and deep formations, the Delaware Basin seismicity is attributed to the poroelastic stresses at seismogenic depth caused by the shallow sandstone injections, which have the opposite sign to and a larger magnitude than stress changes from the fractured shale extractions. The poroelastic stress magnitude is larger for injection because of the smaller sandstone hydraulic diffusivity.

Understanding the origin of induced earthquakes can guide extraction and disposal operations. For example, the induced seismic hazard can be minimized by injecting fluids into porous sediments (52) rather than a low-porosity basement (28). Diffusive seismicity with rapid spatial decay associated with injection into the low-porosity basement rocks is mostly due to fracturing, where injection pressure exceeds the minimum principal stress and rock tensile strength (28). The smaller footprint

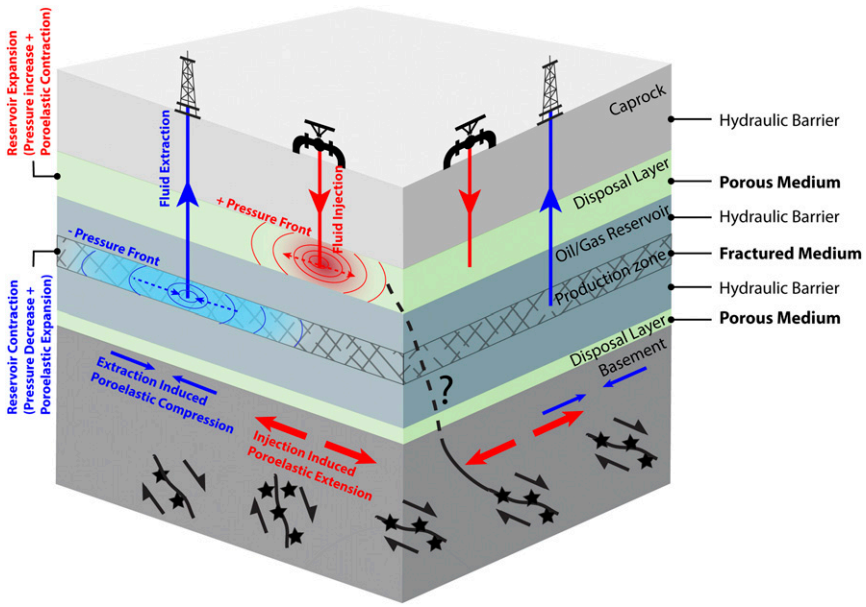

Fig. 4. Schematic summarizing the physical processes associated with fluid injection and extraction. Injection in the shallow disposal layer, characterized by smaller hydraulic diffusivity, causes larger extensional poroelastic response within the basement. Extraction in the fractured shale, characterized by larger hydraulic diffusivity, causes smaller compressional poroelastic response within the basement. The basement and unfractured shale share similar poroelastic processes due to fluid injection and extraction. Fluid pathways connecting the shallow disposal layer and deep basement may locally increase the basement fluid pressure.

of seismicity results from high rock strength or a lack of critically stressed faults within the zone of significant poroelastic stresses. Thus, because of the larger poroelastic response, injection into less porous formations (e.g., basement) can be more hazardous if major faults are present.

Better knowledge of the subsurface stress evolution is key to forecasting fault reactivation and assessing seismic hazards due to industrial activities (3, 47, 53). Despite improvements in seismic monitoring capacity and the resulting decrease in the magnitude detection threshold (54), identifying the dominant mechanism responsible for induced seismicity requires integrating subsurface geology with physical models. Since pore pressure is commonly invoked as the main driver for injection-induced seismicity, with poroelastic stresses being of secondary importance, our Delaware Basin results demonstrate that poroelastic stresses can, in some cases, be the dominant stress change inducing earthquakes. This observation is provided in the context of an unconventional hydrocarbon production area, which is characterized by massive shallow injections. Thus, our results may be of particular relevance to seismic activity induced at depth by shallow anthropogenic activity. As the future energy demands increase globally (55), dealing with the enormous amount of coproduced wastewater remains challenging, and safe shallow injection for disposal is more cost-efficient than deep injection or water treatment (11). As the primary mechanism recognized in this study, poroelastic stresses could also be relevant to proactively design shallow injection strategies, observe crustal stress change, and assess earthquake potential. These processes may help inform other human activities, such as geothermal exploration, CO_2 sequestration, and natural gas underground storage.

Methods

Coupled Poroelastic Modeling. We employ a coupled poroelastic model to calculate the spatial and temporal evolution of poroelastic stresses and pore pressure due to fluid injection and extraction. The theory of poroelasticity accounts for the coupling between the porous medium's deformation and the pore fluid pressure evolution. Fully coupled, linear poroelasticity includes a set of governing equations that describe fluid–solid (Eq. **1**) and solid–fluid (Eq. **2**) couplings. The governing equations relating the deformation field $\boldsymbol{u}$ and pore pressure p, both of which are a function of position $\boldsymbol{x}$ and time t, are given by (27, 32)

$$G\nabla\cdot\nabla\boldsymbol{u}+\frac{G}{1-2\vartheta}\nabla(\nabla\cdot\boldsymbol{u})-\alpha\nabla p=0, \quad [1]$$

$$\frac{1}{Q}\frac{\partial p}{\partial t}+\alpha\frac{\partial(\nabla\cdot\boldsymbol{u})}{\partial t}-\nabla\cdot(\chi\nabla p)=q(\boldsymbol{x},t), \quad [2]$$

where ∇ is the gradient operator and $\nabla\cdot$ is the divergence operator, G is the shear modulus, ϑ is the drained Poisson's ratio, α is the Biot's effective stress coefficient, Q is the Biot's modulus, χ is the mobility coefficient defined by the ratio of intrinsic permeability and dynamic fluid viscosity, and q is the volumetric fluid injection rate per unit bulk volume. To characterize a linear poroelastic medium, five independent parameters are needed, including G, ϑ, undrained Poisson's ratio ϑ_u, hydraulic diffusivity D, and Skempton's pore pressure coefficient B. Parameters α, χ, and Q can be uniquely determined using these five parameters (27). The list of model parameter values for the seven Earth layers is shown in *SI Appendix*, Table S1. The system of governing Eqs. 1 and **2** is solved by imposing mechanical boundary conditions of zero traction and flow boundary conditions of zero excess pore pressure at the half-space surface (56). Additional details about model setup and implementation are given in *SI Appendix*, SI Text.

InSAR Data Processing. We apply a multitemporal SAR interferometric analysis (57, 58) to a set of 93 SAR images acquired by the Sentinel-1A/B C-band satellites between September 2016 and December 2020 in descending path 85 (heading ~192.8° and average incidence ~39.6°) (*SI Appendix*, Table S2). We coregister the single look complex (SLC) images to the image acquired on 28 June 2018, using a standard matching algorithm and subsequent enhanced spectral diversity (58). Next, we apply a multilooking factor of 32 and 6 in range and azimuth, respectively, which increases the signal-to-noise ratio and yields SLC images with a pixel dimension of ~75 m × 75 m. We generate 372 high-quality interferograms using this dataset. We use the Shuttle Radar Topography Mission Digital Elevation Model (59) and precise satellite orbital information to remove the topographic phase. We perform a statistical test on the time series of complex interferometric phase noise to identify less noisy ones with robust phase observations (57). Next, we apply a sparse phase unwrapping using a minimum cost flow algorithm (60) to obtain absolute phase changes. We apply a filter based on two-dimensional (2D) wavelet multiresolution to correct the spatially correlated atmospheric delay (61). To solve for the surface deformation time series, we use a reweighted least-squares approach (57). Finally, we reduce residual atmospheric errors by applying a high-pass filter to each pixel's time series (57). The long-term line-of-sight displacement rates are the slope to the best-fitting line of the surface deformation time series. Description of the deformation rate map is given in *SI Appendix*, SI Text.

Modeling of Elastic Load. We adopt the numerical solution of the 3D elastic response of a spherical, layered non–self-gravitating Earth (62) to an arbitrary normal force load in the radial direction at depth. We consider the displacements and the stress components given the Preliminary Earth Reference Model (63). The Green's functions, relating loads to strain tensors, are calculated using STATIC1D modified to account for radial force loadings for a spherical Earth (45, 62). Through a forward modeling procedure, the strain tensor at depth can be calculated using

$$\epsilon=\boldsymbol{GL}, \quad [3]$$

where ϵ is the distributed strain tensor; $\boldsymbol{G}$ is the Green's function; and $\boldsymbol{L}$ is the distributed force loading at depth, which is the equivalent gravity converted from the reported fluid volumes at wells. More details about elastic loading and CFS calculation are provided in *SI Appendix*, SI Text.

Data Availability. Previously published data were used for this work. All data are available in the public domains or in the reference list. Injection and production records are available at https://rrc.texas.gov/resource-center/research/research-queries/. The TexNet earthquake catalog can be obtained at https://coastal.beg.utexas.edu/texnetcatalog/#!/. SAR images are obtained through the Alaska Satellite Facility at https://search.asf.alaska.edu/#/.

ACKNOWLEDGMENTS. We gratefully acknowledge funding support from US Department of Energy Grant DE-SC0019307 to G.Z., M.S., and M.M. We thank Jens-Erik Lund Snee, Kyung Won Chang, Grace Carlson, Hilary Martens, and Roland Bürgmann for discussions. Computation and modeling are partly supported by Savio at the University of California, Berkeley.

1. G. R. Foulger, M. Wilson, J. Gluyas, B. R. Julian, R. Davies, Global review of human-induced earthquakes. *Earth Sci. Rev.* **178**, 438–514 (2018).
2. F. Grigoli *et al.*, Current challenges in monitoring, discrimination, and management of induced seismicity related to underground industrial activities: A European perspective. *Rev. Geophys.* **55**, 310–340 (2017).
3. W. L. Ellsworth, Injection-induced earthquakes. *Science* **341**, 1225942 (2013).
4. K. M. Keranen, M. Weingarten, Induced seismicity. *Annu. Rev. Earth Planet. Sci.* **46**, 149–174 (2018).
5. G. Zhai, M. Shirzaei, M. Manga, Elevated seismic hazard in Kansas due to high-volume injections in Oklahoma. *Geophy. Res. Let.* **47**, e2019GL085705 (2020).
6. J. L. Rubinstein, A. B. Mahani, Myths and facts on wastewater injection, hydraulic fracturing, enhanced oil recovery, and induced seismicity. *Seismol. Res. Lett.* **86**, 1060–1067 (2015).
7. F. Kolawole *et al.*, The susceptibility of Oklahoma's basement to seismic reactivation. *Nat. Geosci.* **12**, 839–844 (2019).
8. J. Haffener, X. Chen, K. Murray, Multiscale analysis of spatiotemporal relationship between injection and seismicity in Oklahoma. *J. Geophys. Res.* **123**, 8711–8731 (2018).
9. Z. Fan, P. Eichhubl, P. Newell, Basement fault reactivation by fluid injection into sedimentary reservoirs: Poroelastic effects. *J. Geophys. Res.* **124**, 7354–7369 (2019).
10. M. Weingarten, S. Ge, J. W. Godt, B. A. Bekins, J. L. Rubinstein, Induced seismicity. High-rate injection is associated with the increase in U.S. mid-continent seismicity. *Science* **348**, 1336–1340 (2015).
11. B. R. Scanlon, R. C. Reedy, F. Male, M. Walsh, Water issues related to transitioning from conventional to unconventional oil production in the Permian Basin. *Environ. Sci. Technol.* **51**, 10903–10912 (2017).
12. T. Hincks, W. Aspinall, R. Cooke, T. Gernon, Oklahoma's induced seismicity strongly linked to wastewater injection depth. *Science* **359**, 1251–1255 (2018).
13. C. Frohlich *et al.*, Onset and cause of increased seismic activity near Pecos, West Texas, United States, from observations at the Lajitas TXAR Seismic Array. *J. Geophys. Res.* **125**, e2019JB017737 (2020).

14. R. J. Skoumal, A. J. Barbour, M. R. Brudzinski, T. Langenkamp, J. O. Kaven, Induced seismicity in the Delaware Basin, Texas. *J. Geophys. Res.* **125**, e2019JB018558 (2020).
15. B. R. Scanlon, M. B. Weingarten, K. E. Murray, R. C. Reedy, Managing basin-scale fluid budgets to reduce injection-induced seismicity from the recent US shale oil revolution. *Seismol. Res. Lett.* **90**, 171–182 (2019).
16. A. Savvaidis, B. Young, G. D. Huang, A. Lomax, TexNet: A statewide seismological network in Texas. *Seismol. Res. Lett.* **90**, 1702–1715 (2019).
17. R. J. Skoumal *et al*., The induced Mw 5.0 March 2020 West Texas seismic sequence. *J. Geophys. Res.* **126**, e2020JB020693 (2021).
18. S. Tung, G. Zhai, M. Shirzaei, Potential link between 2020 Mentone, West Texas M5 earthquake and nearby wastewater injection: Implications for aquifer mechanical properties. *Geophys. Res. Lett.* **48**, e2020GL090551 (2021).
19. A. Savvaidis, A. Lomax, C. Breton, Induced seismicity in the Delaware Basin, West Texas, is caused by hydraulic fracturing and wastewater disposal. *Bull. Seismol. Soc. Am.* **110**, 2225–2241 (2020).
20. S. C. Maxwell, Hydraulic fracture height growth. *CSEG Rec.* **36**, 18–22 (2011).
21. K. Fisher, N. Warpinski, Hydraulic-fracture-height growth: Real data. *SPE Prod. Oper.* **27**, 8–19 (2012).
22. F. Deng, T. H. Dixon, S. Xie, Surface deformation and induced seismicity due to fluid injection and oil and gas extraction in western Texas. *J. Geophys Res.* **125**, e2019JB018962 (2020).
23. Y. Guglielmi, F. Cappa, J. P. Avouac, P. Henry, D. Elsworth, Induced seismicity. Seismicity triggered by fluid injection-induced aseismic slip. *Science* **348**, 1224–1226 (2015).
24. M. R. Brown, S. Ge, Small earthquakes matter in injection-induced seismicity. *Geophys. Res. Lett.* **45**, 5445–5453 (2018).
25. P. Segall, Earthquakes triggered by fluid extraction. *Geology* **17**, 942–946 (1989).
26. P. Segall, S. Lu, Injection-induced seismicity: Poroelastic and earthquake nucleation effects. *J. Geophys. Res.* **120**, 5082–5103 (2015).
27. R. J. Wang, H. J. Kümpel, Poroelasticity: Efficient modeling of strongly coupled, slow deformation processes in a multilayered half-space. *Geophysics* **68**, 705–717 (2003).
28. T. H. W. Goebel, E. E. Brodsky, The spatial footprint of injection wells in a global compilation of induced earthquake sequences. *Science* **361**, 899–904 (2018).
29. L. Johann, S. A. Shapiro, C. Dinske, The surge of earthquakes in central Oklahoma has features of reservoir-induced seismicity. *Sci. Rep.* **8**, 11505 (2018).
30. J. R. Rice, M. P. Cleary, Some basic stress diffusion solutions for fluid-saturated elastic porous media with compressible constituents. *Rev. Geophys. Space Phys.* **14**, 227–241 (1976).
31. H. F. Wang, *Theory of Linear Poroelasticity with Applications to Geomechanics and Hydrogeology* (Princeton Univ. Press, Princeton, NJ, 2000), p. 276.
32. A. H.-D. Cheng, *Poroelasticity* (Springer, 2016), p. 865.
33. J. D. Hyman *et al*., Understanding hydraulic fracturing: A multi-scale problem. *Philos. Trans. R. Soc. Math. Phys. Eng. Sci.* **374**, 20150426 (2016).
34. D. T. Birdsell, H. Rajaram, D. Dempsey, H. S. Viswanathan, Hydraulic fracturing fluid migration in the subsurface: A review and expanded modeling results. *Water Resour. Res.* **51**, 7159–7188 (2015).
35. J. E. Lund Snee, M. D. Zoback, Multiscale variations of the crustal stress field throughout North America. *Nat. Commun.* **11**, 1951 (2020).
36. K. W. Chang, P. Segall, Injection-induced seismicity on basement faults including poroelastic stressing. *J. Geophys. Res.* **121**, 2708–2726 (2016).
37. P. Segall, Stress and subsidence resulting from subsurface fluid withdrawal in the epicentral region of the 1983 Coalinga Earthquake. *J. Geophys. Res.* **90**, 6801–6816 (1985).
38. J.-M. Kim, R. R. Parizek, Numerical simulation of the Noordbergum effect resulting from groundwater pumping in a layered aquifer system. *J. Hydrol.* **202**, 231–243 (1997).
39. S. Staniewicz *et al*., InSAR reveals complex surface deformation patterns over an 80,000 km^2 oil-producing region in the Permian Basin. *Geophys. Res. Lett.* **47**, e2020GL090151 (2020).
40. J. Furnans *et al*., "Identification of the vulnerability of the major and minor aquifers of Texas to subsidence with regard to groundwater pumping" (Texas Water Development Board, 2017).
41. J. E. Meyer, M. R. Wise, S. Kalaswad, "Pecos Valley Aquifer, West Texas: Structure and Brackish Groundwater" (Texas Water Development Board, 2012).
42. N. Z. Dvory, M. D. Zoback, Does prior depletion affect the occurrence of earthquakes induced by hydraulic fracturing in the Delaware Basin of Texas and New Mexico? *American Geophysical Union Annual Fall Meeting* (2019), p. S11B-03.
43. W. E. Farrell, Deformation of the earth by surface loads. *Rev. Geophys. Space Phys.* **10**, 761–797 (1972).
44. G. Carlson, M. Shirzaei, S. Werth, G. Zhai, C. Ojha, Seasonal and long-term groundwater unloading in the Central Valley modifies crustal stress. *J. Geophys. Res.* **125**, e2019JB018490 (2020).
45. C. W. Johnson, Y. Fu, R. Bürgmann, Seasonal water storage, stress modulation, and California seismicity. *Science* **356**, 1161–1164 (2017).
46. K. M. Keranen, M. Weingarten, G. A. Abers, B. A. Bekins, S. Ge, Induced earthquakes. Sharp increase in central Oklahoma seismicity since 2008 induced by massive wastewater injection. *Science* **345**, 448–451 (2014).
47. G. Zhai, M. Shirzaei, M. Manga, X. Chen, Pore-pressure diffusion, enhanced by poroelastic stresses, controls induced seismicity in Oklahoma. *Proc. Natl. Acad. Sci. U.S.A.* **116**, 16228–16233 (2019).
48. X. Chen *et al*., Temporal correlation between seismic moment and injection volume for an induced earthquake sequence in central Oklahoma. *J. Geophys. Res.* **123**, 3047–3064 (2018).
49. C. Langenbruch, M. D. Zoback, How will induced seismicity in Oklahoma respond to decreased saltwater injection rates? *Sci. Adv.* **2**, e1601542 (2016).
50. D. W. Eaton, *Passive Seismic Monitoring of Induced Seismicity: Fundamental Principles and Application to Energy Technologies* (Cambridge University Press, 2018).
51. H. Lim *et al*., The 2017 Mw 5.5 Pohang earthquake, South Korea, and poroelastic stress changes associated with fluid injection. *J. Geophys. Res.* **125**, e2019JB019134 (2020).
52. M. R. Brown, S. Ge, A. F. Sheehan, J. S. Nakai, Evaluating the effectiveness of induced seismicity mitigation: Numerical modeling of wastewater injection near Greeley, Colorado. *J. Geophys. Res.* **122**, 6569–6582 (2017).
53. M. Shirzaei, W. L. Ellsworth, K. F. Tiampo, P. J. González, M. Manga, Surface uplift and time-dependent seismic hazard due to fluid injection in eastern Texas. *Science* **353**, 1416–1419 (2016).
54. N. Deichmann, D. Giardini, Earthquakes induced by the stimulation of an enhanced geothermal system below Basel (Switzerland). *Seismol. Res. Lett.* **80**, 784–798 (2009).
55. Energy Information Administration, International energy outlook. Office of Energy Analysis within US Department of Energy (2020).
56. G. Zhai, M. Shirzaei, Fluid injection and time-dependent seismic hazard in the Barnett Shale, Texas. *Geophys. Res. Lett.* **45**, 4743–4753 (2018).
57. M. Shirzaei, A wavelet-based multitemporal DInSAR algorithm for monitoring ground surface motion. *IEEE Geosci. Remote Sens. Lett.* **10**, 456–460 (2013).
58. M. Shirzaei, R. Bürgmann, E. J. Fielding, Applicability of Sentinel-1 terrain observation by progressive scans multitemporal interferometry for monitoring slow ground motions in the San Francisco Bay Area. *Geophys. Res. Lett.* **44**, 2733–2742 (2017).
59. T. G. Farr *et al*., The shuttle radar topography mission. *Rev. Geophys.* **45**, RG2004 (2007).
60. M. Costantini, A novel phase unwrapping method based on network programming. *IEEE Trans. Geosci. Remote Sens.* **36**, 813–821 (1998).
61. M. Shirzaei, R. Bürgmann, Topography correlated atmospheric delay correction in radar interferometry using wavelet transforms. *Geophys. Res. Lett.* **39**, L01305 (2012).
62. F. F. Pollitz, Coseismic deformation from earthquake faulting on a layered spherical earth. *Geophys. J. Int.* **125**, 1–14 (1996).
63. A. Dziewoński, D. L. Anderson, Preliminary reference earth model. *Phys. Earth Planet. Inter.* **25**, 297–356 (1981).